

COMPARISON OF RESISTANCE-BASED STRAIN GAUGES AND FIBER BRAGG  
GRATINGS IN THE PRESENCE OF ELECTROMAGNETIC INTERFERENCE  
EMITTED FROM AN ELECTRIC MOTOR

By

Douglas Keller Jr.

A Dissertation Submitted in Partial Fulfillment of the Requirements  
for the Degree of  
Master of Science  
in  
Mechanical Engineering

University of Alaska Fairbanks

Dec 2018

APPROVED:

Dr. Javier Fochesatto, Thesis Advisor

Dr. Rorik Peterson, Committee Chair

Dr. Cheng-fu Chen, Committee Member

Dr. Rorik Peterson, Chair

*Department of Mechanical Engineering*

Dr. Douglas Goering, Dean

*College of Engineering and Mines*

Dr. Michael Castellini, *Dean of the Graduate School*

# Abstract

This thesis reports a performance analysis of resistance based strain gauges and fiber optic fiber Bragg gratings in an environment contaminated by high levels of electromagnetic interference. The obtained results are directly applicable to the development of aerospace vehicles propelled by electrical motors. An area of importance in this relatively new technology is characterizing the mechanical loadings coming off a propulsion device in a stationary setup. This characterization is usually accomplished through the utilization of load cells. The majority of the load cells used in such an application are based on measurements acquired through resistance strain gauges. However, electric motors are known to radiate electromagnetic interference (EMI), which in the case of brushless DC motors is pulsing, alternating, square waves. This EMI severely degrades the signal produced by the resistance strain gauge. This degradation is due to the gauge's metallic construction, acting as an antenna for the EMI. To evaluate the performance of alternative strain measuring methods, a load cell implementing both the resistance strain gauge and fiber Bragg grating sensor, the latter of which is immune to EMI, was designed as a test article. The load cell was calibrated and demonstrated a thrust load sensitivity of  $1.93 \pm 0.04$  lbf through the strain gauge system and  $0.56 \pm 0.56$  lbf through the fiber Bragg grating system. The device was subjected to both mechanical loading and EMI to quantify the effect of the EMI on the resistance strain gauge. Testing of the device included operating a brushless DC motor, with a coupled flywheel, attached to the load cell at a range of angular velocities from 500 to 2400 RPM. During laboratory testing the resistance strain gauge signal exhibited an important amount of signal spikes and electrical noise, introduced by the EMI contamination; the fiber Bragg grating did not. The spikes increased linearly with the speed of the motor. The electrical noise required bandpass filtering to extract the mechanical signal, which was obtained without noise in the fiber Bragg grating signal. The resistance strain gauge signal, at a maximum, had a signal to noise ratio of 0.0443; the fiber Bragg grating signal, at a minimum, had a signal to noise ratio of 2.0114. These results demonstrated the fiber Bragg grating is more applicable in an EMI contaminated environment.



# Table of Contents

	Page
<b>Title Page . . . . .</b>	<b>i</b>
<b>Abstract . . . . .</b>	<b>iii</b>
<b>Preface . . . . .</b>	<b>ix</b>
<b>1 Background . . . . .</b>	<b>1</b>
1.1 Scope . . . . .	1
1.2 The Experiment . . . . .	3
1.3 Electromagnetic Interference . . . . .	4
1.4 Load Cells . . . . .	5
1.4.1 Hydraulic Load Cells . . . . .	5
1.4.2 Pneumatic Load Cells . . . . .	7
1.4.3 Strain Gauge Load Cells . . . . .	7
1.5 Strain Sensors . . . . .	8
1.5.1 Electrical Resistance Strain Gauges . . . . .	8
1.5.2 Fiber Bragg Gratings . . . . .	9
1.6 Wheatstone Bridge . . . . .	10
1.7 Fiber Optic Sensing Systems . . . . .	12
1.7.1 Distributed Sensing . . . . .	12
1.8 Preliminary Load Cell Designs . . . . .	13
1.8.1 Initial Design . . . . .	13
1.8.2 Secondary Design . . . . .	14
<b>References . . . . .</b>	<b>15</b>

<b>2 Comparison of Resistance-Based Strain Gauges and Fiber Bragg Gratings in the Presence of Electromagnetic Interference Emitted from an Electric Motor</b>	<b>17</b>
2.1 Introduction	18
2.2 Methodology	20
2.2.1 Test Apparatus	20
2.2.2 Load Cell Design	23
2.2.3 Calibration	29
2.2.4 Signal Analysis	30
2.3 Results	32
2.4 Discussion	36
2.5 Conclusion	37
<b>3 Concluding Statement</b>	<b>41</b>
<b>4 Appendix</b>	<b>43</b>
4.1 MATLAB Code	43
4.1.1 Load Cell Analytical Stress, Strain, and Resolution	43
4.1.2 Load Cell Calibration Script	44
4.1.3 Fiber Bragg Grating Data Loader	44
4.1.4 Foil Gauge Data Loader	46
4.1.5 Motor Noise Data Loader	47
4.1.6 Signal to Noise Ratio Calculations	48
4.1.7 Despiking Program	49

# List of Figures

	Page
1 NASA Helios Prototype . . . . .	1
2 NASA Airvolt Test Stand . . . . .	2
3 Square wave pulse supplied to the Q100-5L brushless DC motor . . . . .	5
4 Location of the oscilloscope probe . . . . .	6
5 Square wave pulse supplied to the Q100-5L brushless DC motor . . . . .	6
6 A common foil strain gauge with its size attributes labeled . . . . .	8
7 Fiber Bragg grating . . . . .	10
8 Wheatstone bridge circuit . . . . .	11
9 Setup to measure and monitor fiber Bragg grating sensors . . . . .	12
10 Initial load cell design . . . . .	14
11 Secondary load cell design . . . . .	15
12 The electromagnetic interference emitted by the Q100-5L motor . . . . .	19
13 Experimental setup and layout . . . . .	21
14 The test stand . . . . .	21
15 Arrangement of the flywheel, motor, load cell, and test stand . . . . .	22
16 The load cell design . . . . .	23
17 Load cell design with a small plane unit square . . . . .	25
18 SolidWorks stress simulation . . . . .	26
19 SolidWorks strain simulation . . . . .	26
20 Half-bridge Wheatstone bridge circuit . . . . .	27
21 NASA's Wavelength Division Multiplexing Fiber Optic Sensing System. . . . .	28
22 The load cell placed in the Instron Model 4400 . . . . .	29
23 Resulting calibration best fit lines . . . . .	30
24 The fiber Bragg grating response . . . . .	33
25 The frequency domain series of the fiber Bragg grating response . . . . .	33

26	The foil gauge response . . . . .	34
27	The frequency domain series of the foil gauge response . . . . .	34
28	The motor EMI and foil gauge signal . . . . .	35
29	The spikes per second . . . . .	35

## List of Tables

	Page
1 Instruments used in the testing apparatus. . . . .	3
2 Instruments used in the testing apparatus. . . . .	22
3 Mechanical properties of Aluminum 2024 T351 . . . . .	24
4 Foil gauge and fiber Bragg grating characteristics . . . . .	27
5 Resolution of the two strain measurement systems on the load cell. . . . .	29
6 Filter specifications . . . . .	31
7 Spikes per second at the corresponding motor RPM. . . . .	33
8 Signal to noise ratio of all the datasets . . . . .	36

## Preface

This research came about through an internship with the National Aeronautics and Space Administration (NASA). I was funded by the Alaska Space Grant Program (ASGP) to go to the NASA Armstrong Flight Research Center in Edwards, California, after my junior year of undergraduate studies. I was assigned to work at NASA's Fiber Optic Sensing System (FOSS) Lab to investigate the heat transfer characteristics of an enclosure to contain the FOSS. The setup was to be integrated into the Quiet Supersonic Transport aircraft, now known as the X-59. The center's main campus is on the Edwards Air Force Base, but at the time the FOSS Lab was off campus at the Palmdale court houses. While I was there, James Murray, a NASA engineer from main campus, came by the lab with an idea for an experiment with the FOSS. I expressed my interest and found myself on board. Paul Bean, my NASA mentor for my internship, enabled the processes for my involvement, with the help of the FOSS Lab's head Allen Parker. I used part of the experiment, designing a load cell, as my Senior Project with my teammate Daniel Eagan. The development of the effect of electromagnetic interference (EMI) on foil strain gauges compared to fiber Bragg gratings, and system integrations therein, I used for my thesis presented here.

A big thanks to the Alaska Space Grant Program for the initial opportunity to be exposed to this project and to NASA for providing the funding for this project. Another big thanks to James Murray for his patience and guidance through this joint venture. I owe a lot of gratitude to Dr. Javier Fochesatto for his mentorship and advising throughout my graduate and undergraduate studies. I am very grateful for Dr. Cheng-fu Chen, with his comments and wisdom on my research and on my studies. I am also very thankful for Dr. Rorik Peterson's support throughout this experience. My gratitude continues with help and support I received from Paul Bean, who structured and arranged this project behind the scenes, thereby enabling its existence, and from Patrick Chan and Allen Parker, for their expertise, continuing assistance, and support. And, of course, I appreciate my family and friends, who had the understanding and patience to allow me to put forth my best effort in this endeavor.



Figure 1: NASA Helios Prototype aircraft. Notice the multiple electric motors distributed along the wing [6].

# 1 Background

## 1.1 Scope

The scope of this experiment is to look at the effects of electromagnetic interference (EMI) on traditional, commonly used foil strain gauges, within the realm of their application to electrical propulsion in aerospace. This research is important because the use of electrical motors is becoming much more prevalent in the field of transportation, providing a multitude of potential benefits. This includes electrically powered flight, research into which has been largely led by the National Aeronautics and Space Administration (NASA). For example, the NASA X-57 Maxwell is a top-wing aircraft completely powered by small, distributed, electrical motors [9]. Further examples of NASA led research include the Pathfinder, Pathfinder Plus [7], Centurion,[8] Helios Prototype (Figure 1),[6] the Leading-Edge Asynchronous Propeller Technology (LEAPTech), the Hybrid-Electric Integrated Systems Testbed (HEIST) Ironbird, the Scalable Convergent Electric Propulsion Technology and Operations Research (SCEPTOR), and the Airvolt test stand[17, 15] shown in Figure 2. In essence, aerospace is a strong and upcoming area of electric motor application.

In general, when testing propulsion technologies, understanding the full ensemble of load-



Figure 2: NASA Airvolt Test Stand. NASA’s propulsion device test stand to investigate the use of electric motors in aviation [14].

ings, especially thrust and torque, and their effects, like vibration, produced during propulsion is extremely important to aerostructure design and the quantification of induced stress. Ignoring these mechanical perturbations can result in disastrous effects [2]. Initially, to determine these loadings and the consequential effects on aerostructures, test stands are used to evaluate the propulsion devices on the ground in a controlled environment [17, 4]. However, a few experiments running an electric motor coupled to a propeller on the Airvolt test stand revealed that the torque and thrust data gathered from the testing were covered in excessive noise. This excessive noise was attributed to the EMI produced by the electric motor [17]. The load cells used to obtain the loadings were strain gauge based load cells,[17] which measure strain with foil strain gauges to infer the loadings. In this particular scenario, the foil gauges were immersed in significant EMI from the electric motor, resulting in severely degraded signal performance, requiring further sophisticated signal processing to be utilized.

This thesis work focuses on evaluating the NASA Fiber Optic Sensing System (FOSS) with fiber Bragg gratings as an alternative to the use of traditional foil strain gauges to completely avoid the risk associated with EMI contamination. The evaluation was performed through laboratory experiments, simultaneously subjecting foil strain gauges and the fiber Bragg gratings to varying mechanical loadings. The testing demanded the fabrication of a mechanical stand to host the electrical motor and the loadings in position, as well as the

Table 1: Instruments used in the testing apparatus.

Item	Manufacturer and Model
Flywheel	1961 Ford Falcon Flywheel 21.41 lbf 10.8 in Diameter
Brushless DC Electric Motor	Hacker Motor Q100-5L 11 kW 28 poles
Motor Controller	JETI SPIN Pro 300 Opto
Battery	MaxAmps Lithium-Polymer 10900 mAh 6S 22.2 V
Servo Controller	Hitec HFP-30
Secondary Motor Controller	JETI JETIBOX
Fiber Bragg Grating Interrogator	NASA WDM FOSS
DC Power Supply	Agilent 6614C 0-100 V 0-0.5 A
Amplifier	Advanced Research Instruments Corp. DC-100
Oscilloscope	Tektronix TDS3032B
Laptops	Windows 10 OS, Windows 7 OS

load cell with the strain sensors attached. Moreover, it was necessary to prepare circuitry to couple the foil gauges to the instrumentation and prepare software to capture the signals obtained from both strain sensors simultaneously. Special attention was paid to the thermal drift on the foil strain gauges and fiber Bragg gratings.

## 1.2 The Experiment

To investigate that the EMI from an electric motor is indeed affecting foil gauge data, an experiment, utilizing a brushless DC electric motor (see Table 1 for the motor model and make) coupled to a load cell with two types of strain sensors, was undertaken. The first type of sensor is the classic foil gauge and the second is the fiber Bragg grating (FBG). FBGs are based on a dielectric material that does not conduct EMI, differing them from foil gauges. A flywheel was mounted to the motor to provide dynamic loading while retaining static thrust loads (from the weight of the flywheel) for the load cell to measure. See Section 2.2.1 for a detailed setup of the experiment. Essentially, this setup provides an experiment where both sensors measure the same mechanical loadings and are immersed in the same EMI. Then the foil gauge response was compared to the EMI immune FBG response, and the effect of EMI was quantified.

### 1.3 Electromagnetic Interference

Electromagnetic interference is the high frequency electromagnetic perturbation that is emitted by electrical or electromechanical systems that have not been adequately shielded. Due to this inadequacy, these systems emit EMI to nearby space and devices. Some devices can be shielded/grounded in a way to reduce the amount of captured EMI to a negligible effect. However, not all devices are prepared nor capable of this design treatment and return degraded performance. This degradation in sensors is generally seen in the output signal and is qualified as “noise” [16]. However, the term “noise” is commonly used to describe stochastic or random fluctuations of the electromagnetic field. For a common example of stochastic noise, when listening to the radio in the car, during certain times while driving you may notice “fuzziness” or “scratchiness” in the audio, sometimes to point that discerning the words or music is impossible. This is due to the stochastic noise (for more information see [16]). But in this experiment, the noise comes from a very distinct and deterministic signal of the motor operating at a given angular velocity. This noise shows up quite clearly in the sensor output signal and is not random. This distinction is important for mathematically processing the signal.

As stated before, the EMI is produced by other electronics. In the case of the research presented here, the source is the brushless DC electric motor. The noise coming from this type of electric motor is the alternating square wave pulse coursing through the large copper coils in the motor, generating the magnetic field to rotate the motor rotor. This square wave is clearly visible in Figure 3, which was captured by operating the motor and placing the oscilloscope probe near it (without contact; see Figure 4) with the oscilloscope sampling at 10000 points per 200  $\mu$ seconds (normally described as 50 MS/s, where S is samples and s is second; see Table 1 for the oscilloscope model). However, care must be taken when sampling a periodic signal, as an aliasing frequency[5] demonstrated in Figure 5 can occur. The signal in Figure 5 is the square wave pulse sampled at 10 kS/s. To capture the true square wave form, the oscilloscope has to sample at twice the rate of the square wave pulsing. But when measuring strain, the sampling rate must be much lower to capture the lower frequencies where the mechanical loadings can be found in this experiment. When this happens, the

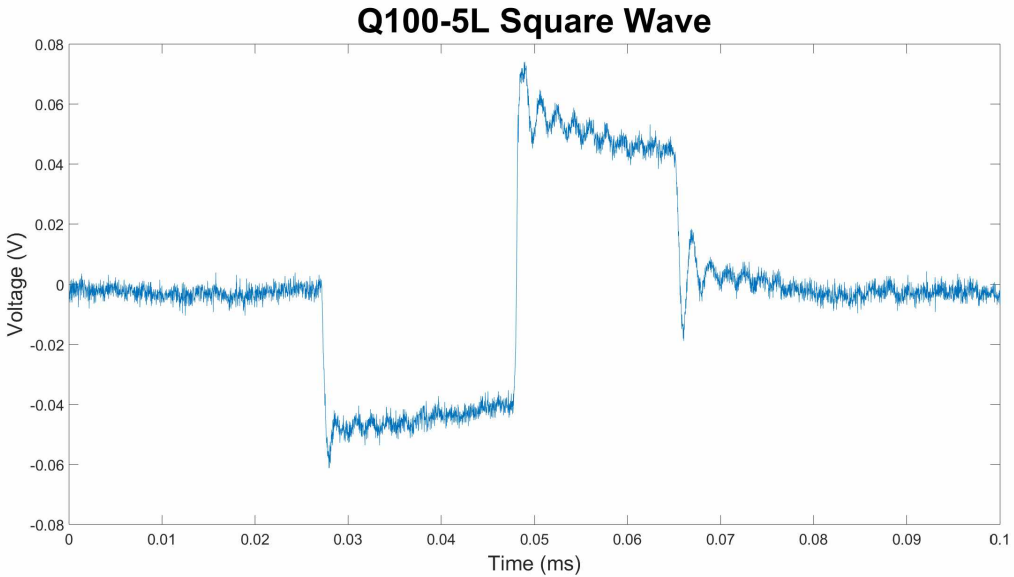


Figure 3: Square wave pulse supplied to the Q100-5L brushless DC motor. Captured by the Tektronix TDS3032B oscilloscope. Sampled at 50 MS/s with the motor running at 1600 rpm.

square waves look like a series of spikes, clouding the strain signal in noise.

## 1.4 Load Cells

In this section, a brief review is given on what load cells are, with a few examples from industry. Load cells are devices that are used to measure loadings such as forces and torques, hence the “load” in “load cell”. Applications range from scales to measure weight, determining thrust from engine and propeller arrangements, to monitoring large structure health. Currently, there are three major types of load cells that exist for commercial application: hydraulic load cells, pneumatic load cells, and strain gauge load cells.

### 1.4.1 Hydraulic Load Cells

Hydraulic load cells are fluid-based pressure sensors that rely on a force balance to convert an applied load into a consistent, measurable signal. In a hydraulic load cell, the load of interest is applied to a piston, which compresses a filling liquid contained in a diaphragm chamber, increasing its pressure. The pressure of the filling liquid is then measured and compared against calibration data to determine the applied load. While hydraulic load cells

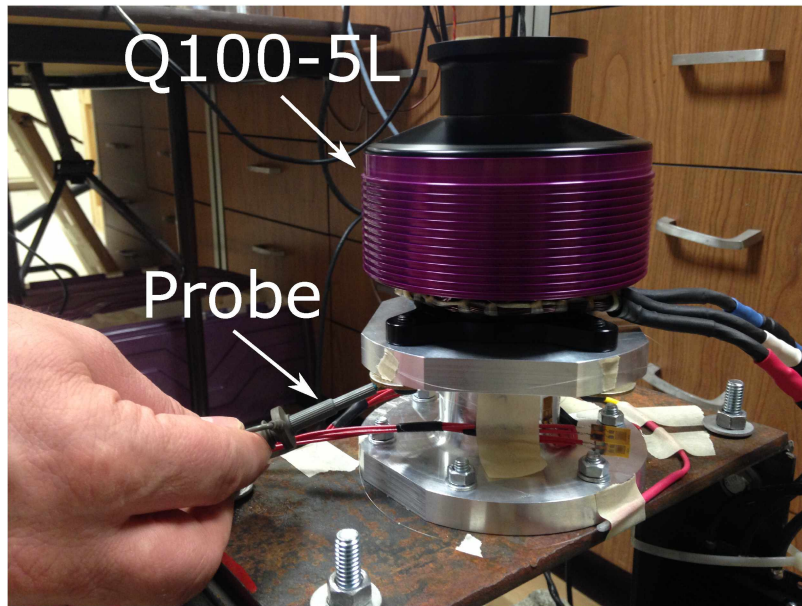


Figure 4: Location of the oscilloscope probe when measuring the Q100-5L brushless DC motor EMI.

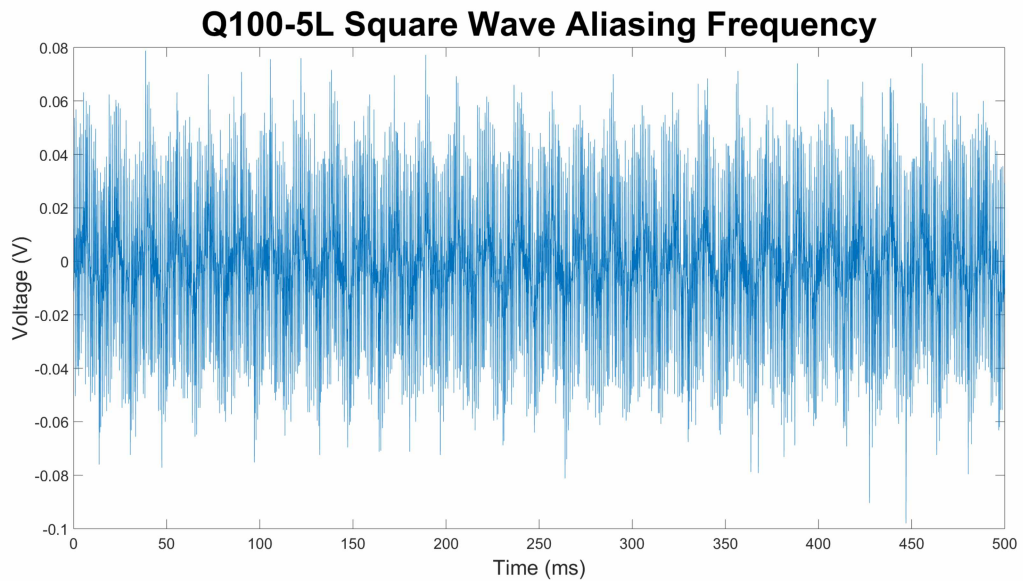


Figure 5: Square wave pulse supplied to the Q100-5L brushless DC motor, yet sampled at 10 kS/s by the Tektronix TDS3032B oscilloscope. A severe aliasing frequency occurs.

can give accurate results for static loads and contain no electrical components, they are slow to respond due to the viscosity of the filling liquid. This makes measuring dynamic or cyclic loads challenging with this type of load cell. Additionally, the weight of the filling liquid makes these devices heavy, restricting the scope of their application.

### 1.4.2 Pneumatic Load Cells

Pneumatic load cells operate on the same force balance principle as the hydraulic load cells. However, they are filled with gas, such as air or nitrogen, with several dampening chambers with a diaphragm that are compressed with a loaded piston. Major advantages of pneumatic load cells include high accuracy for small loads, cleanliness (lack of liquids to leak and damage equipment or skew results), and insensitivity to temperature variations. Conversely, like hydraulic load cells, the filling gas has viscosity which leads to slow response times. Additionally, the diaphragms used in these devices are capable of rupturing, and they require clean, dry gas to function properly.

### 1.4.3 Strain Gauge Load Cells

Strain gauge load cells, as their name implies, use a combination of strain gauges to measure loads. These load cells are essentially deformable objects that are stressed with an applied load. This stress results in a strain throughout the load cell. The strain gauges are mounted to the load cell structure in a specific orientation so that a load applied can be calculated based on the resulting strain, which is proportional to the loading. This type of load cell almost exclusively uses foil strain gauges (see Section 1.5.1) to measure the strain. These load cells are extremely accurate in static and dynamic loading applications, as they function with a surface coupled resistor that lacks noticeable hysteresis. Their disadvantage is that they require many electrical components for accurate readings and, because of this, are highly susceptible to EMI, causing noise and error in the resulting data if EMI is present [17]. The strain gauge load cell is the most commonly used load cell variant in the aerospace industry, due to their dynamic loading measuring ability and their low weight in comparison to the other available types.

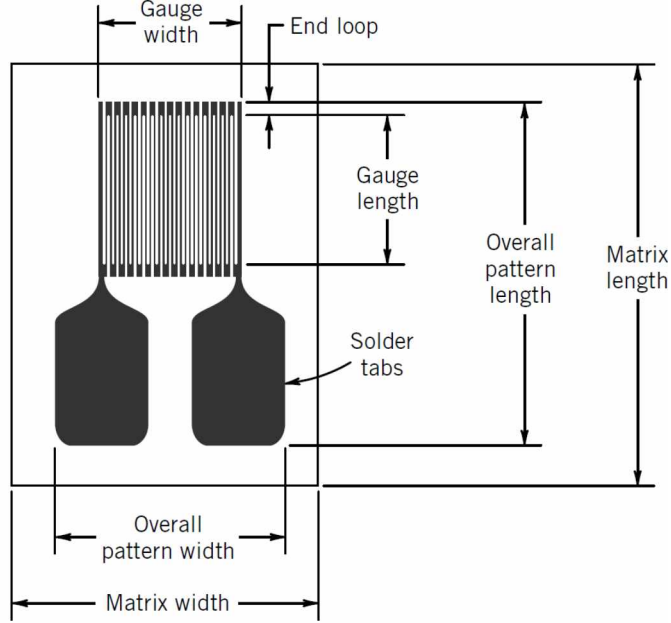


Figure 6: A common foil strain gauge with its size attributes labeled. Borrowed from *Figliola 2011* [5].

## 1.5 Strain Sensors

### 1.5.1 Electrical Resistance Strain Gauges

Electrical resistance strain gauges, or foil gauges (gage is a common alternative to gauge in industry and may be used instead) as they will be referred to from here on, are perhaps the most common strain sensors in use today. They are essentially metallic wire resistors that change resistance under a given applied loading or strain. Foil gauges receive the name from their manufacturing process. A metal foil is photoetched to produce a grid-like wire pattern. Figure 6 shows a standard example of a foil gauge. To relate the applied strain to resistance, the change in resistance of a wire undergoing strain is given as:[3, 5]

$$\frac{dR/R}{\varepsilon} = 1 + 2\nu + \frac{d\rho/\rho}{\varepsilon} \quad (1)$$

Where  $R$  is the resistance of the uniform conductor (metal wire),  $dR$  is the change in resistance due to the applied strain,  $\varepsilon$ .  $\rho$  is the specific resistance,  $d\rho$  is the change in specific resistance, and  $\nu$  is the Poisson's ratio, both intrinsic properties of the material used for the

gauge. However, strain gauge manufacturers relate the relative change in resistance to strain for their products with the constant known as the gauge factor,  $GF$ , which is described by the following relation:[3, 5]

$$GF = \frac{\Delta R/R}{\varepsilon} \approx \frac{dR/R}{\varepsilon} \quad (2)$$

When this gauge is connected to a voltage source and an appropriate accompanying circuit, the change in resistance produces a change in current allowing this change to be traced through the circuit's output voltage. Because this measurements implies the determination of a current in a low impedance sensor the most appropriate and commonly used circuit is the Wheatstone bridge [3, 5] (see Section 1.6).

### 1.5.2 Fiber Bragg Gratings

Fiber Bragg Gratings (FBGs) are etchings made in a fiber optic cable by means of a ultraviolet laser that engraves a phased change in fiber core refractive index (see Figure 7). This procedure results with an etching in the fiber that reflects a particular wavelength of light (see Figure 9) and transmits the rest ([11, 13, 10] and references therein). In this way, the fiber Bragg grating acts as a notch filter in reflection and transmits the rest of the spectrum. The wavelength of light reflected is known as the Bragg or resonant wavelength. FBGs measure strain by producing a measurable shift in the Bragg wavelength reflected when the sensor is strained (see Figure 9). The change in the reflected wavelength is proportional to the strain applied, conveyed in the following equation:[11, 13, 10]

$$\Delta\lambda \approx 0.78\lambda\varepsilon \quad (3)$$

Where  $\Delta\lambda$  is the shift in Bragg wavelength and  $\lambda$  is the Bragg wavelength of the unstressed FBG.  $\varepsilon$  is the strain applied to the FBG. Generally, FBGs are fabricated to reflect a wavelength around 1550 nm when unstrained. Therefore, a light source that provides suitable intensities of light at the unstrained reflected wavelength and throughout the range of reflected wavelengths possible due to strain is important to retrieve readable strain measurements.

The effect of temperature change of the fiber core material also has to be considered when observing shifts in the Bragg wavelength. The shift of the Bragg wavelength is dominated by

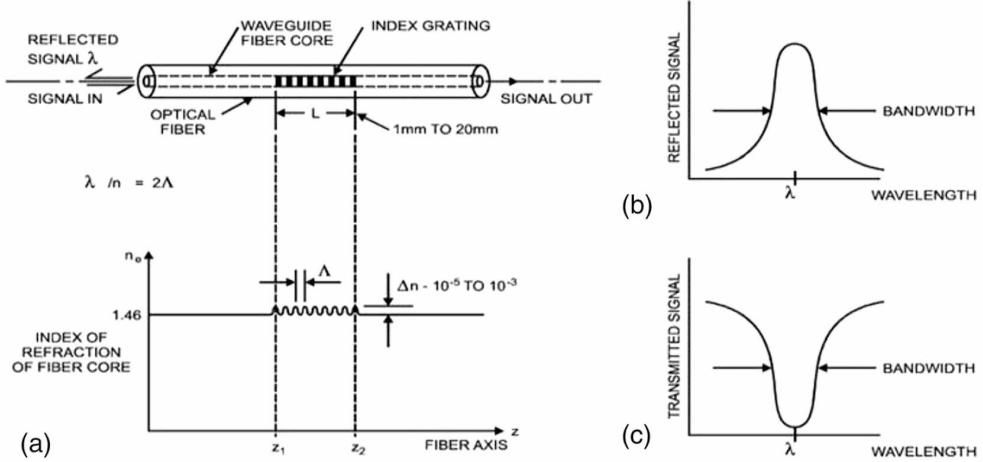


Figure 7: Fiber Bragg grating. a) is a description of the FBG, b) is the spectrum of the wavelengths reflected by the FBG, and c) is the spectrum of wavelengths transmitted.  $\lambda$  is the Bragg wavelength,  $n$  and  $\Delta n$  is the refractive index and its change over the grating, respectively.  $\Lambda$  is the period of the grating, and  $L$  is the grating length. Borrowed from Krohn 2014[11].

the change in refractive index due to a change in temperature, as seen by the following:[11, 10]

$$\Delta\lambda \approx 6.67 \times 10^{-6} \frac{1}{^{\circ}\text{C}} \lambda \Delta T \quad (4)$$

Where  $\Delta T$  is the change in temperature of the fiber core material. Since the applied strain,  $\varepsilon$ , generally occurs in the range of few hundred  $\mu\varepsilon$ , the temperature response of the fiber refractive index alone can be greater, shown by Eq. 4. Note that this is only the change in the Bragg wavelength due to the temperature change experienced by the fiber core material. When in application, the change in Bragg wavelength from the strain due to the thermal expansion[18] of the material that the FBG is affixed to also occurs. This thermally induced strain appears in Eq. 3 as part of the applied strain  $\varepsilon$ .

## 1.6 Wheatstone Bridge

Solving for  $\Delta R$  in Eq. 2, the change in resistance is small because the strain to be measured is generally small. To retrieve the weak signal produced by the small change in resistance of the foil gauge under strain, an accompanying circuit needs to be implemented. A common circuit for foil gauge application is the Wheatstone bridge (Figure 8). The

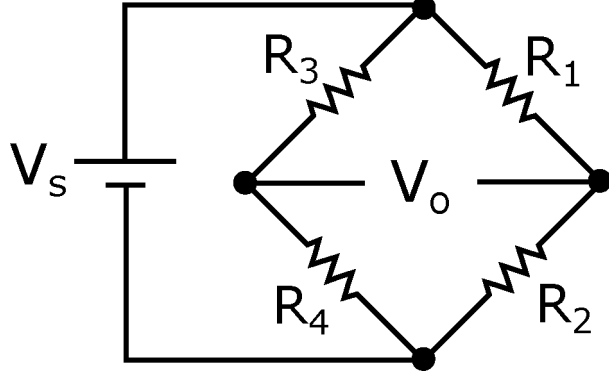


Figure 8: Wheatstone bridge circuit.  $V_o$  is the bridge output voltage, and  $V_s$  is the bridge excitation voltage.  $R_n$ , where  $n = 1 \sim 4$ , are the bridge resistances/gauges.

Wheatstone bridge output with a single gauge as  $R_1$  is described by the following relation:[5, 3]

$$V_o + \Delta V_o = V_s \frac{(R_1 + \Delta R_1)(R_4 - R_3 R_2)}{(R_1 + \Delta R_1 + R_2)(R_3 + R_4)} \quad (5)$$

Where  $V_o$  is bridge output voltage,  $\Delta V_o$  is the change in bridge output voltage, and  $V_s$  is the bridge excitation voltage.  $R_1$  is the foil gauge resistance and  $\Delta R_1$  is the change of foil gauge resistance when a strain is applied. If the bridge is initially balanced without strain applied, then  $V_o = 0$  and the change in resistance of the foil gauge is directly represented by the bridge output voltage change  $\Delta V_o$ .

Different arrangements of the Wheatstone bridge with different numbers of foil gauges are possible and are called quarter, half, and full-bridge arrangements. These arrangements can boost the Wheatstone bridge signal output to levels measurable by an oscilloscope. Eq. 5 represents the quarter bridge case with a single gauge. For the other two cases, the following can describe the bridge response[5] when multiple foil gauges with the same gauge factor are used:

$$\Delta V_o = \frac{GF}{4} (\varepsilon_1 - \varepsilon_2 - \varepsilon_3 + \varepsilon_4) V_s \quad (6)$$

Where  $\varepsilon_n$ , as  $n = 1 \sim 4$ , is the applied strain at the respective foil gauges  $R_1$  through  $R_4$  in Figure 8.  $GF$  is the common gauge factor for the foil gauges described in Section 1.5.1. As Eq. 6 conveys, the change in bridge output voltage can be increased with more gauges. For the research at hand, the half bridge circuit was used.

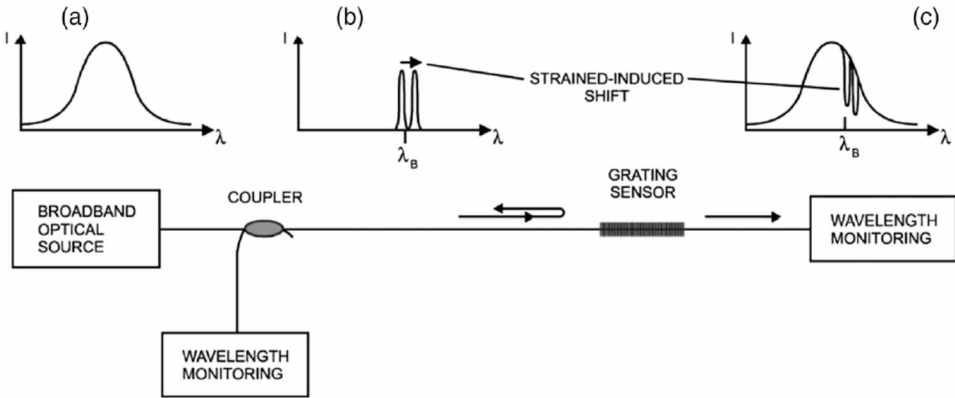


Figure 9: Setup to measure and monitor fiber Bragg grating sensors. The broadband optical source is the light or laser that is used to excite the fiber. The wavelength monitoring device tracks the response of the Bragg wavelength of the fiber Bragg grating. a) is the light injected into the fiber, b) is the Bragg wavelength reflected by the sensor, and c) are the wavelengths transmitted by the sensor. Figure borrowed from *Krohn 2014* [11].

## 1.7 Fiber Optic Sensing Systems

When using a FBG to measure strain, an accompanying system, similar to the Wheatstone bridge circuit to the foil gauge, is necessary. The general setup requires a light source, the FBG, and a way to monitor the FBG's response, usually a spectrometer of some sort (see Figure 9). An integrated system to do this is generally referred to as a FBG Interrogator. For this research, NASA's FOSS was used as the FBG Interrogator.

### 1.7.1 Distributed Sensing

Fiber optic sensing systems allow more effective ways to measure multiple points at once when compared to foil gauge systems. This ability is typically called Distributed Sensing in industry. This ability arises from the potential to place multiple FBGs on a single fiber that share a common interrogating instrument. This isn't possible with foil gauges as a Wheatstone bridge circuit is needed at every strain measurement point, producing a cumbersome and complex system.

Different schemes allow for multiple FBGs to be monitored at approximately the same time. One method is known as wavelength division multiplexing (WDM),[12, 11, 10] where multiple FBGs with different resonant wavelengths are etched into a fiber to measure different

desired measurands, such as temperature or strain. A broadband optical source (also called a white light) injects a broad spectrum light into the fiber, encompassing all the FBG resonant wavelengths with their potential shifts. A spectrometer reads the reflected signals and the FBGs are tracked by their initial resonant wavelength. The NASA FOSS used in this research uses this scheme to measure strain and temperature simultaneously.

Another scheme which can be layered on top of the WDM is called time division multiplexing (TDM) [12, 11, 10]. TDM uses the timing between the light pulses down the fiber and the reflections back from the FBGs to determine their spatial positioning and is used in other NASA FOSSs [1]. When both schemes are used together, hundreds of sensors can be monitored at approximately the same time, only limited by the fiber and sensor attenuation on the pulsed light source.

## 1.8 Preliminary Load Cell Designs

This research necessitates the design of a load cell that implements both the fiber sensing technology and the foil strain gauge technology to measure mechanical loadings. Commercially, there are no load cells that utilize fiber sensing technology. Therefore, it is needed to engineer a load cell to accommodate FBGs. At first, a design able to measure all potential forces and moments along and about each of the three axes was desired for future testing beyond the scope of this thesis. This was reduced to a design capable of measuring just a single force along a single axis, to reduce cost. The final design found in Section 2.2.2 retained this design trait and only measured thrust during testing.

### 1.8.1 Initial Design

The initial design of the load cell was a central hub with three arms in radial symmetry (see Figure 10). The arms are rectangular in cross-section with filleted edges. The arms are mounted to a test stand with the central hub subjected to the intended loading. This allows the loading to be experienced through the arms. The strain sensors are placed on the arms to measure the strain caused by the stress from the loading. The strain measurements, combined with the elastic modulus of the arm material, allow for the determination of the

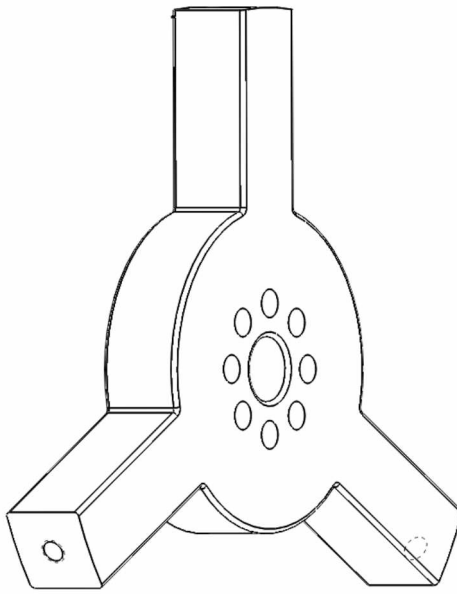


Figure 10: Initial load cell design with the radially symmetrical arms for strain sensing and central hub for load application.

measured stress. The measured stress is combined with the geometry and placement of the loading to determine the magnitude of the loading, thereby measuring it. Each arm is treated as a beam subjected to bending superimposed with a square shaft subjected to torque. To solve this arrangement, the plane stress is solved for [18]. However, this design requires 8 sensors per arm to solve for the stresses and one sensor for temperature, resulting in 25 sensors needed for the device overall. For the scope of this thesis and considering the cost of the sensors, this design was deemed excessive and a new design was made.

### 1.8.2 Secondary Design

The next design proposed the use of a single arm from the initial three-arm design, modeling the load cell as a bending beam (Figure 11). This design met the requirement to reduce the complexity and degrees of freedom from the previous design, requiring only one sensor to measure the thrust and another to measure temperature. However, due to the bending of the beam as the load is applied, a strain gradient is induced in the beam material; this is much more difficult to measure and analyze with fiber sensing technology. Due to the

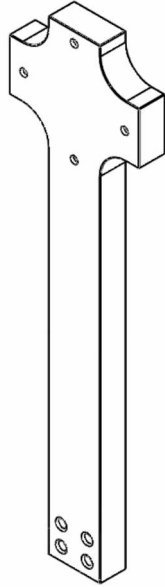


Figure 11: Secondary load cell design. A crucifix design based off of one of the arms from the initial design.

required length of the FBG ( $\sim$ 1 inch), this strain differential would be nearly impossible to avoid and would produce inaccurate readings, leading to the final design in Section 2.2.2.

## References

- [1] Chan, H. M., Parker, A. R., Piazza, A., and Richards, W. L., in *2015 IEEE Avionics and Vehicle Fiber-Optics and Photonics Conference* (Santa Barbara, California, 2015).
- [2] CRGIS, N. L., “Flutter Tests of the Full Span Lockheed Electra,” Youtube (1960).
- [3] Dally, J. W. and Riley, W. F., *Experimental Stress Analysis*, 3rd ed. (College House Enterprises, LLC, Knoxville, Tennessee, 1991).
- [4] Dusen, M. V., “The World’s Largest Jet Engine Starts Certification Testing,” (2017).
- [5] Figliola, R. S. and Beasley, D. E., *Theory and Design for Mechanical Measurements*, 5th ed. (John Wiley & Sons, Inc., Hoboken, New Jersey, 2011).
- [6] Galante, N., “NASA Helios Prototype,” (2001).

- [7] Gibbs, Y., “Past Projects: Pathfinder / Pathfinder Plus Solar-Powered Aircraft,” (2010).
- [8] Gibbs, Y., “NASA Armstrong Fact Sheet: Centurion Remotely Piloted Solar-Powered Airplane,” (2014).
- [9] Gibbs, Y., “NASA Armstrong Fact Sheet: NASA X-57 Maxwell,” (2018).
- [10] Kersey, A. D., Davis, M. A., Patrick, H. J., LeBlanc, M., Koo, K. P., Askins, C. G., Putnam, M. A., and Friebele, E. J., Journal of Lightwave Technology **15**, 1442 (1997).
- [11] Krohn, D., MacDougall, T., and Mendez, A., *Fiber Optic Sensors: Fundamentals and Applications*, 4th ed. (Society of Photo-Optical Instrumentation Engineers, Bellingham, Washington, 2014).
- [12] Krohn, D. A., *Fiber Optic Sensors: Fundamentals and Applications*, 2nd ed. (Instrument Society of America, Research Triangle Park, North Carolina, 1992).
- [13] Lee, B., Optical Fiber Technology **9**, 57 (2003).
- [14] Levine, J. and Hughes, L., “Electric Motor Test Stand Will Help With Future X-planes,” (2016).
- [15] Obringer, L., “Electric Propulsion Technologies,” (2017).
- [16] Ott, H. W., *Noise Reduction Techniques in Electronic Systems*, 2nd ed. (John Wiley & Sons, Inc., New York, 1988).
- [17] Samuel, A. and Lin, Y., in *51st AIAA/SAE/ASEE Joint Propulsion Conference* (Orlando, Florida, 2015).
- [18] Solecki, R. and Conant, R. J., *Advanced Mechanics of Materials* (Oxford University Press, New York, New York, 2003).

## **2 Comparison of Resistance-Based Strain Gauges and Fiber Bragg Gratings in the Presence of Electromagnetic Interference Emitted from an Electric Motor**

Douglas Keller Jr., Daniel R. Eagan, Gilberto J. Fochesatto, Rorik Peterson

### **Abstract**

Recently, electric motors have been investigated in depth for their application in aerospace. One area of importance is on the characterization of the loadings from a propulsion device in a stationary setup. This characterization is usually accomplished through the utilization of load cells. The majority of the load cells used in this application are designed around a resistance-based strain gauge. However, electric motors radiate electromagnetic interference (EMI) when in operation; pulsing, alternating, square waves in the case of brushless DC motors. This interference degrades the strain sensor information retrieved through the strain gauge, due to the gauge's metallic construction, acting as an antenna for the EMI.

To evaluate the performance of strain gauge sensors against fiber Bragg gratings, the latter of which are immune to EMI, a load cell implementing both sensor technologies was designed as a test platform subjected to the same mechanical loading and interference to quantify EMI's effect for aerospace applications. The load cell had a sensitivity of  $1.93 \pm 0.04$  lbf through the strain gauge system and  $0.56 \pm 0.56$  lbf through the fiber Bragg grating system. The strain gauge signal contained the mechanical loading signal embedded in wideband noise and an important density of spikes. The fiber Bragg gratings did not have spikes and had little noise. The strain gauge signal, at a maximum, had a signal to noise ratio, the mean divided by the standard deviation, of 0.0443 at 500 RPM; the fiber Bragg grating signal, at a minimum, had a signal to noise ratio of 2.0114 at 1000 RPM. Therefore, on the basis of the mechanical tests performed in this work, the recommended sensor of choice for electric propulsion in aerospace applications is the fiber Bragg grating.

## 2.1 Introduction

The increasing viability of electric propulsion for ground-based applications has prompted investigation into electric propulsion for aerospace use. Part of this investigation involves the stationary testing and research of electric motors, such as with the NASA's Airvolt electric motor test stand [11]. Current knowledge of testing aviation motors draws on the historical use of combustion engines and therefore the experimental data collection of electric motors isn't as readily available. As a result, NASA's Airvolt testing has determined problematic areas in data collection; one such area is the mitigation of electromagnetic interference (EMI) emitted from the electric motors under testing (demonstrated by Figure 12). This EMI affects the fidelity of the sensors gathering data during testing but also could affect more sensitive guidance and control instrumentation in aerospace, if not properly engineered. Some of the worst affected sensors were the load cells[11] used to collect the thrust and torque loadings created by the motor. The load cells in the experiment used resistance-based strain gauges, commonly referred to as foil gauges as they are etched from a metallic foil, which is the de facto standard for measuring strains in load sensing applications.

This paper aims to demonstrate the pervasion of EMI in foil gauge signals and compare them to the strain signals retrieved from fiber Bragg gratings (FBGs) through load cell measurements made in the framework of electrical motors for aerospace development. However, currently there are no load cells commercially available that utilize FBGs for load measuring. This created a need to develop such a device for this experiment. A load cell, with both foil gauges and FBGs implemented to measure strain, was designed and attached to an electric motor coupled with a flywheel for dynamic mechanical loading. This design subjects both sensors to the same mechanical loading and EMI, allowing for the analysis of the results in terms of EMI contamination.

EMI is the high frequency electromagnetic perturbation emitted from inadequately shielded electronics and/or electromechanical systems. These emissions interact with nearby electronics and can lead to performance degradation if not properly handled [8]. Due to their metallic construction, foil gauges act as antennas and easily capture EMI. Since they must be in physical contact with the object where the strain is measured, this prevents standard ways of

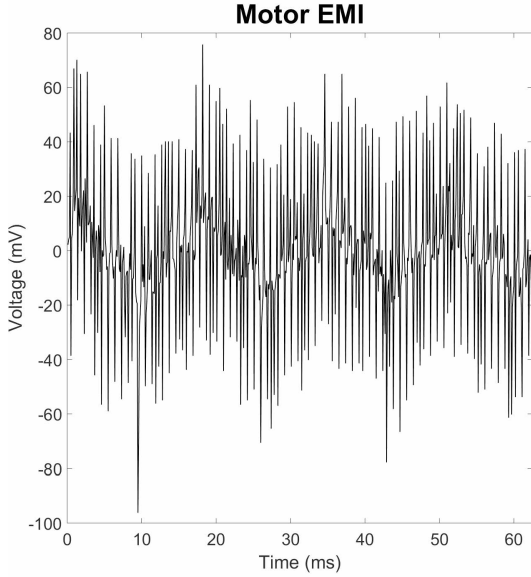


Figure 12: The electromagnetic interference emitted by the Q100-5L motor when operated at 1600 RPM. The EMI was collected with the Tektronix TDS3032B oscilloscope, with the probe held next to, but not contacting, the strain sensors on the load cell.

mitigating external noise, such as shielding, as the sensor cannot be completely surrounded in relation to the motor, and grounding, since this would result in the loss of the signal. In the case of brushless DC electric motors, a common form of electric motors in today's industry, the EMI manifests itself in the alternating voltage square waves resulting from energizing the motor stator coils. When these square waves are sampled at the rates used to measure mechanical loadings, as these are generally at lower frequencies, they take the form found in Figure 12. That is to say, the EMI at this sampling rate, 10 kS/s (S is samples and s is seconds), resembles a series of spikes because it is under sampled at this sampling rate. This will be discussed further in the data analysis.

Foil gauges are sensors that change resistance with an applied strain [3, 2]. They are well known and commonly used in strain sensing applications and in commercially available load cells. They are generally described by a manufacturer supplied constant (responsivity), known as the gauge factor,  $GF$ :

$$GF = \frac{\Delta R/R}{\varepsilon} \quad (7)$$

Where  $R$  is the resistance of the foil gauge and  $\Delta R$  is the change in resistance due to the applied strain,  $\varepsilon$ .

On the other hand, FBGs are etchings in a fiber optic cable, creating a sudden periodic change in the core refractive index [5, 7, 6]. They reflect a particular wavelength, known as the Bragg, or resonance, wavelength, and transmit the rest when subjected to an optical input. When subjected to strain, the Bragg wavelength shifts proportionally, as described by the following equation:[5, 7, 6]

$$\Delta\lambda \approx 0.78\lambda\varepsilon \quad (8)$$

Where  $\Delta\lambda$  is the shift in Bragg wavelength and  $\lambda$  is the Bragg wavelength of the unstrained FBG.  $\varepsilon$  is the strain applied to the FBG. FBGs are immune to EMI,[5, 7, 6] and therefore provide a true mechanical loading reference point to compare against the foil gauges.

This paper is divided into the description of the test apparatus (Section 2.2.1), the design and calibration of the load cell (Section 2.2.2), and the mathematical methods utilized for the signal analysis (Section 2.2.4), followed by the results and discussion (Sections 2.3 and 2.4)

## 2.2 Methodology

### 2.2.1 Test Apparatus

The experimental setup is found in Figure 13 and 14 with the instruments listed in Table 2. The Q100-5L motor, coupled to a flywheel (arrangement in Figure 15), is mounted to the load cell, which is affixed to the stationary test stand. The flywheel provides a known static axial weight for the load cell to sense. The foil gauges from the load cell are connected to a Wheatstone bridge in half-bridge arrangement, which is powered by the high precision and low drift Agilent 6614C DC power supply and is connected to the transimpedance Advanced Research Instruments DC-100 amplifier, DC to 100 MHz low noise, to boost the Wheatstone bridge's small output voltage signal. This small signal is then sampled, digitized, and recorded by the Tektronix TDS3032B digital oscilloscope and transferred to the laptop computer through a high data rate ethernet connection. The power supply, amplifier, and oscilloscope are all grounded to a common ground, removing the EMI from their respective circuits. The FBGs from the load cell are interrogated by the NASA Wavelength Division Multiplexing (WDM) Fiber Optic Sensing System (FOSS), with the data transferred by

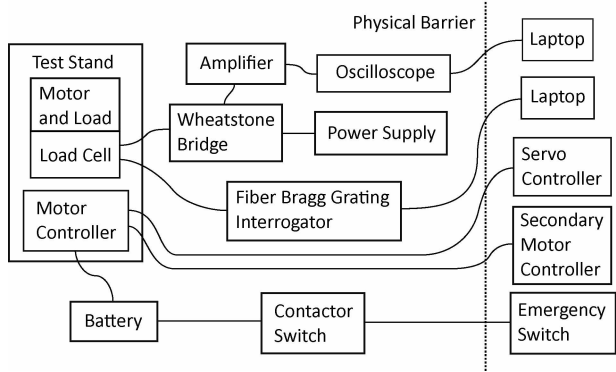


Figure 13: Experimental setup and layout. A physical barrier was used to separate the data acquisition and motor control from the running motor and test stand.

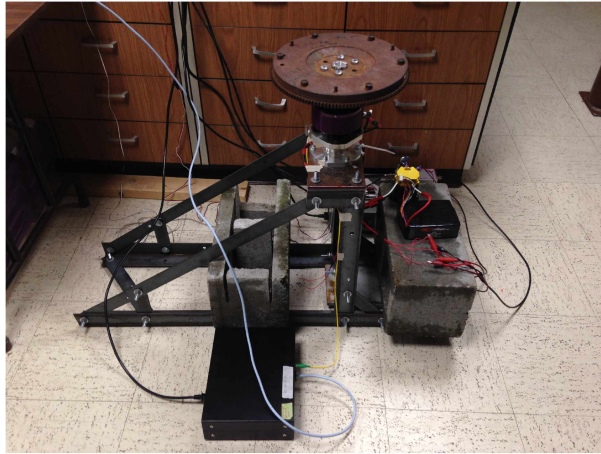


Figure 14: The test stand with the load cell and motor/flywheel attached.

ethernet to a separate laptop computer.

The motor is controlled primarily by the JETI SPIN Pro 300 Opto motor controller, assisted by the secondary JETI JETIBOX controller. The main motor controller supplies the square wave to the motor, while the secondary controller regulates the ramping up of the power delivered to the motor. This was done to protect the motor and act as a current limiter on motor start up. The motor's speed and activation are manually controlled by the HFP-30 servo controller. The MaxAmps 6s LiPo battery is connected to the main motor controller, powering the motor system. To comply with security and safety norms and regulations, a contactor switch in the path between the motor controller and the battery is powered by an auxiliary emergency switch, providing a safeguard mechanism, in case the experiment needs to be halted for any reason.

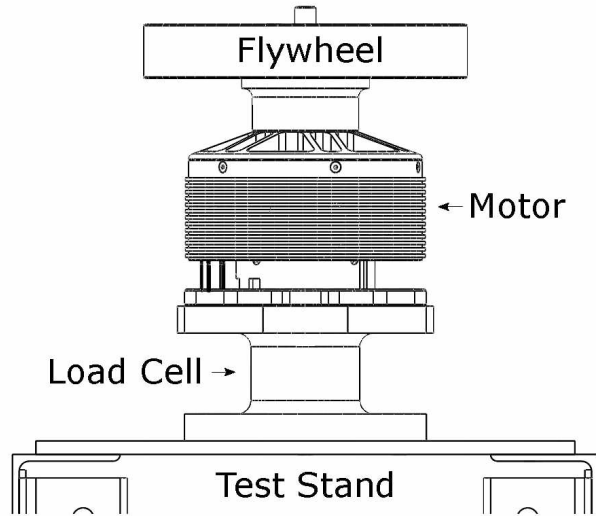


Figure 15: Arrangement of the flywheel, motor, load cell, and test stand in the setup. The flywheel is bolted to the motor, the motor is bolted to the load cell, and the load cell is bolted to the test stand. This provides a path for the force to flow through the load cell.

Table 2: Instruments used in the testing apparatus.

Item	Manufacturer and Model
Flywheel	1961 Ford Falcon Flywheel 21.41 lbf 10.8 in Diameter
Brushless DC Electric Motor	Hacker Motor Q100-5L 11 kW 28 poles
Motor Controller	JETI SPIN Pro 300 Opto
Battery	MaxAmps Lithium-Polymer 10900 mAh 6S 22.2 V
Servo Controller	Hitec HFP-30
Secondary Motor Controller	JETI JETIBOX
Fiber Bragg Grating Interrogator	NASA WDM FOSS
DC Power Supply	Agilent 6614C 0-100 V 0-0.5 A
Amplifier	Advanced Research Instruments Corp. DC-100
Oscilloscope	Tektronix TDS3032B
Laptops	Windows 10 OS, Windows 7 OS

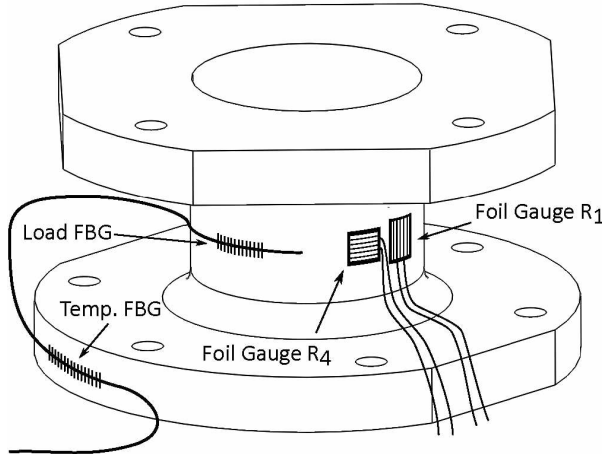


Figure 16: The load cell design featuring a top 4 bolt flange and a bottom 6 bolt flange with sensor placement on the cylinder wall and bottom flange.

### 2.2.2 Load Cell Design

The experiment required a load cell able to measure thrust (tensile force) up to 80 lbf, while withstanding a combined loading of 80 lbf of tensile force and 150 lbf-in of torque. The design of the load cell is a hollow cylinder with a wall thickness of 0.01 in and has flanges for mounting on either end (see Figure 16) and was machined from aluminum alloy 2024 T351. Thrust is measured through the longitudinal axis. The loading is applied to the top flange (for this experiment the electric motor mounts to top flange with 4 bolts) and the bottom flange is used to mount the load cell to a stationary test stand with 6 bolts (Figure 15). This allows a path for the force to flow through the load cell, resulting in measurable strain. A FBG is placed along the circumference of the cylinder wall, to measure applied loading induced strain, while another FBG is placed on the bottom flange to measure temperature induced strain; both FBGs are on the same fiber, one with a resonant wavelength of 1550nm and the other at 1540nm. Two foil gauges are placed 1 inch away from the FBG on the cylinder wall, one in vertical placement and the other in horizontal placement (see Figure 16 for sensor placement). The FBGs are interrogated with the NASA WDM FOSS, and the foil gauges are in half-bridge arrangement in a Wheatstone bridge (see Figure 20), which is powered by the power supply and measured by the oscilloscope.

Table 3: Mechanical properties of Aluminum 2024 T351 [10].

Elastic Modulus $E$	10700 ksi
Poisson's Ratio $\nu$	.33
Thermal Expansion Coefficient $\alpha$	$12.45 \times 10^{-6} \text{ } ^\circ F^{-1}$
Yield Stress	52 ksi
Infinite Cyclic Fatigue Limit	11.1 ksi

### 2.2.2.1 Stress and Strain Analysis

For the load cell to retrieve the thrust, the cylinder is compressed or stretched along its longitudinal axis, resulting in a normal stress along this axis. The FBG and foil gauge placed horizontally along the circumference of the cylinder wall experience the imposed strain from the normal stress through Poisson's ratio. The vertically placed foil gauge experiences the strain from the normal stress directly (see Eq. 9 versus Eq. 10). To calculate the thrust from the measurement, the strain is related to the force acting on the cross section with the following equations:[13, 15]

$$\varepsilon_v = \frac{\sigma}{E} = \frac{P}{AE} \quad (9)$$

$$\varepsilon_h = \nu \varepsilon_v \quad (10)$$

Where  $\varepsilon_v$  is the measured strain from the vertically mounted foil gauge and  $\varepsilon_h$  is the measured strain from the horizontally mounted sensors.  $\sigma$  is the normal stress imposed by the force (thrust)  $P$ , with the given cylinder cross-sectional area,  $A$ .  $\nu$  is the Poisson's ratio and  $E$  is the elastic modulus of aluminum 2024 (see Table 3 for the properties of aluminum 2024 T351). The calculated vertical and horizontal strain are  $118.4 \times 10^{-6}$  and  $39.1 \times 10^{-6}$  of elongation, respectively, for the applied loading of 80 lbf. Although stress concentrations at the mounting holes and fillets are present, the constant cross section of the main cylinder area, where the strain measuring sensors are mounted, is not affected by this, therefore producing a uniform strain. The aluminum yield stress and cyclic fatigue limit in Table 3 impose constraints for the maximum loading applicable to the load cell. To remain in the elastic range the experienced stress needs to remain below 52 ksi, and to endure infinite cyclic loadings, needs to remain below 11.1 ksi. With the expected maximum combined loading of 80 lbf and 150 lbf-in, the maximum possible experienced stress in the material needed to

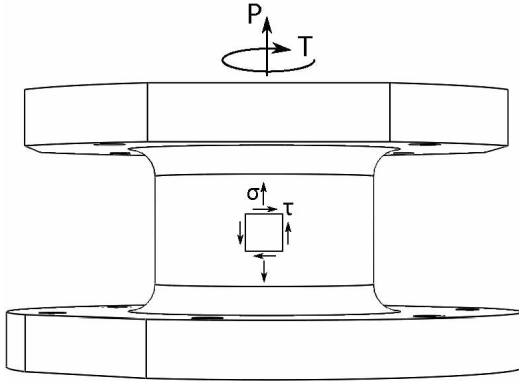


Figure 17: Load cell design with a small plane unit square labeling normal,  $\sigma$ , and shear,  $\tau$ , stresses.  $P$  is the applied thrust and  $T$  is the applied torque.

be determined. For this, the von Mises stress, which is applicable to ductile materials such as aluminum,[4] was utilized. The von Mises stress in a plane can be solved with following relation:[4]

$$\sigma_{vM} = \sqrt{\sigma^2 + 3\tau^2} \quad (11)$$

Where  $\sigma_{vM}$  is the maximum stress experienced or the von Mises stress.  $\sigma$  is the normal stress applied, mentioned earlier, and  $\tau$  is the shear stress applied and is determined by the following:[13, 15]

$$\tau = \frac{Tr}{J} \quad (12)$$

Where  $T$  is the applied torque loading,  $r$  is the outer radius of the cylinder wall, and  $J$  is the polar moment of inertia about the longitudinal axis. The forces and stresses are labeled in Figure 17. With the given maximum expected loadings,  $\sigma_{vM}$  was found to be 4.30 ksi, well below the yield stress and comfortably below the infinite cyclic fatigue limit. Consequently, the maximum thrust load without torque constrained by the fatigue limit is 701 lbf.

To confirm the theoretical calculations, simulations in SolidWorks were performed. The simulations results matched those found analytically. SolidWorks calculated, with the given maximum loadings,  $\sigma_{vM}$  to be 4.28 ksi, practically the same as the analytical result. Figure 18 and 19 show the maximum stress and strain in the vertical direction, respectively. A uniform stress/strain appears on the cylinder of load cell, confirming the previous assumption that the geometrical stress concentrations at the mounting points do not reach the area with the

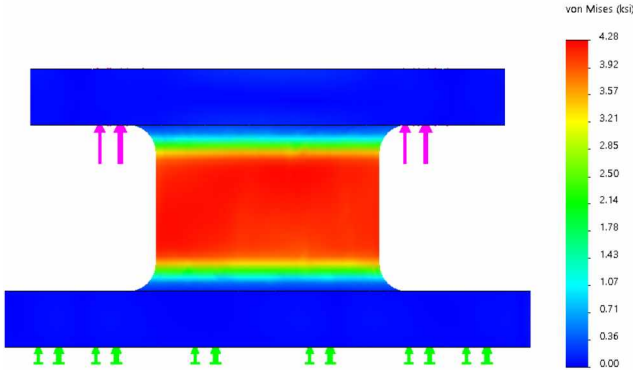


Figure 18: SolidWorks stress simulation result of 80 lbf and 150 lbf-in applied to the 4 top mounting holes. The von Mises stress maxed at 4.28 ksi with a clear uniform stressing of the cylinder wall.

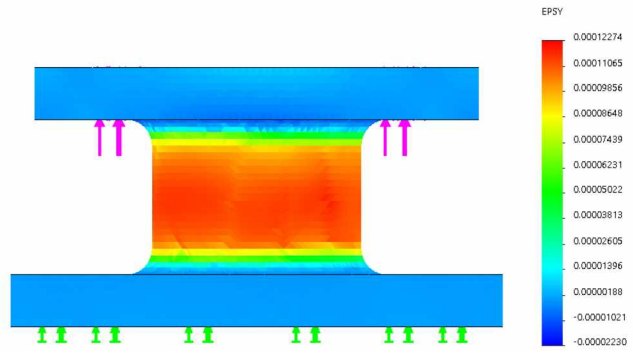


Figure 19: SolidWorks strain simulation of the resultant strain in the vertical direction, labeled EPSY in the figure. A clear, uniform strain is produced in the cylinder wall.

sensors.

#### 2.2.2.2 Strain Measurement

The characteristics of the foil gauges and FBGs are found in Table 4. Both sensors were affixed to the load cell cylinder wall with cyanoacrylate glue; then the free hanging wires/cables were secured to the test stand with tape to prevent movement during motor operation.

To determine the small resistance change in the strained foil gauges, a Wheatstone bridge circuit was used (Figure 20). A half-bridge arrangement was chosen for the circuit design, with  $R_1$  and  $R_4$  as the two foil gauges present on the load cell (refer back to Figure 16).  $R_1$  and  $R_4$  are the vertically and horizontally mounted gauges, respectively.  $R_2$  and  $R_3$  are 330

Table 4: Foil gauge and fiber Bragg grating characteristics

Foil Gauge	
Vendor	Micro-Measurement
Gauge Factor, $GF$	$2.105 \pm 0.5\%$
Resistance, $R$	$350.0 \pm 0.3\%$
Transverse Sensitivity	0.7%
Gauge Width	0.125 in
Gauge Length	0.125 in
Fiber Bragg Grating	
Vendor	NASA Armstrong FOSS Lab
Length	6 mm
Reflectivity	10%
Wavelength	1550 nm, 1540 nm

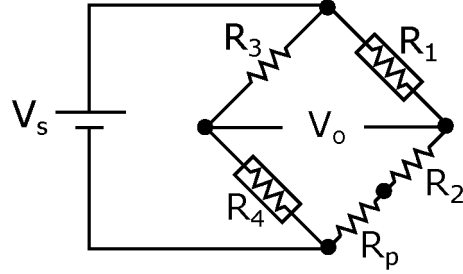


Figure 20: Half-bridge Wheatstone bridge circuit.  $V_o$  is the bridge output voltage, and  $V_s$  is the bridge excitation voltage.  $R_1$  and  $R_4$  are the foil gauges.  $R_p$  is the balancing potentiometer, and  $R_2$  and  $R_3$  are  $330 \Omega$  resistors.

$\Omega$  resistors, and  $R_p$  is a precision potentiometer of  $100 \Omega$  to balance the bridge.

Both gauges experience the same strain,  $\varepsilon_v$ , but  $R_4$  experiences the strain due to Poisson's ratio,  $\varepsilon_h$ , or  $\nu\varepsilon_v$ . The change in the balanced bridge output voltage due to an induced strain on the gauges then can be described as below:[3, 2]

$$\Delta V_o = \frac{GF(1 + \nu)\varepsilon_v}{4} V_s \quad (13)$$

Where  $\Delta V_o$  is the change in bridge output voltage, and  $V_s$  is the bridge excitation voltage.  $GF$  is the gauge factor of the foil gauges described in Eq. 7.  $\varepsilon_v$  is the applied strain in Eq. 9. The oscilloscope samples the amplified bridge response at 10 kS/s. With the motor upper operating speed range of 40 revolutions per second (2400 RPM) at most, this provides a suitable sampling rate to measure the dynamic loadings of the motor/flywheel.



Figure 21: NASA’s Wavelength Division Multiplexing Fiber Optic Sensing System.

NASA’s WDM FOSS (Figure 21) is given as a standalone device for this experiment. Essentially, the device measures the FBGs’ wavelength by injecting a broadband optical source into the sensing fiber. Each FBG on the fiber reflects their Bragg wavelength, 1550 nm and 1540 nm unstrained, for load and temperature measurement respectively, which is measured by an optical spectral analyzer in the WDM FOSS. The peaks of the wavelengths are returned from the system in binary form via ethernet connection from the onboard computer. The system measures the wavelengths at 5 kHz, providing a suitable sampling rate to measure the dynamic loadings present in the test.

### 2.2.2.3 Sensitivity

The sensitivity of the strain measuring systems was determined utilizing Eq. 8 and 13. The Tektronix TDS3032B oscilloscope has a voltage measuring resolution of 1 mV and an accuracy of  $\pm 0.02$  mV. When backtracked through the appropriate equation, the expected force resolution through the foil gauge system is 1.93 lbf, about 2.4% of the maximum expected loading of 80 lbf. NASA’s WDM FOSS has a wavelength measuring resolution of 1 pm and an accuracy of  $\pm 1$  pm. When the load is solved for with Eq. 8, the force resolution is found to be 0.56 lbf, less than 1% of the expected maximum loading, demonstrating a better sensitivity than the foil gauge system. The sensitivities are tabulated in Table 5.

Table 5: Resolution of the two strain measurement systems on the load cell.

Foil Gauges	$1.93 \pm 0.04$ lbf
Fiber Bragg Grating	$0.56 \pm 0.56$ lbf



Figure 22: The load cell placed in the Instron Model 4400 to be loaded in tension for foil gauge system and fiber Bragg grating system calibration.

### 2.2.3 Calibration

The load cell was calibrated with an Instron Model 4400 tensile loading machine in a controlled environment laboratory (see Figure 22). The load cell was quasi-statically loaded in tension from 0 to 500 lbf in roughly 5 lbf steps to produce a large data pool to assign a best fit linear regression model. Figure 23 shows the results of the model fitting. The FBG response is less variable, most likely due to the higher sensitivity provided by the NASA WDM FOSS.

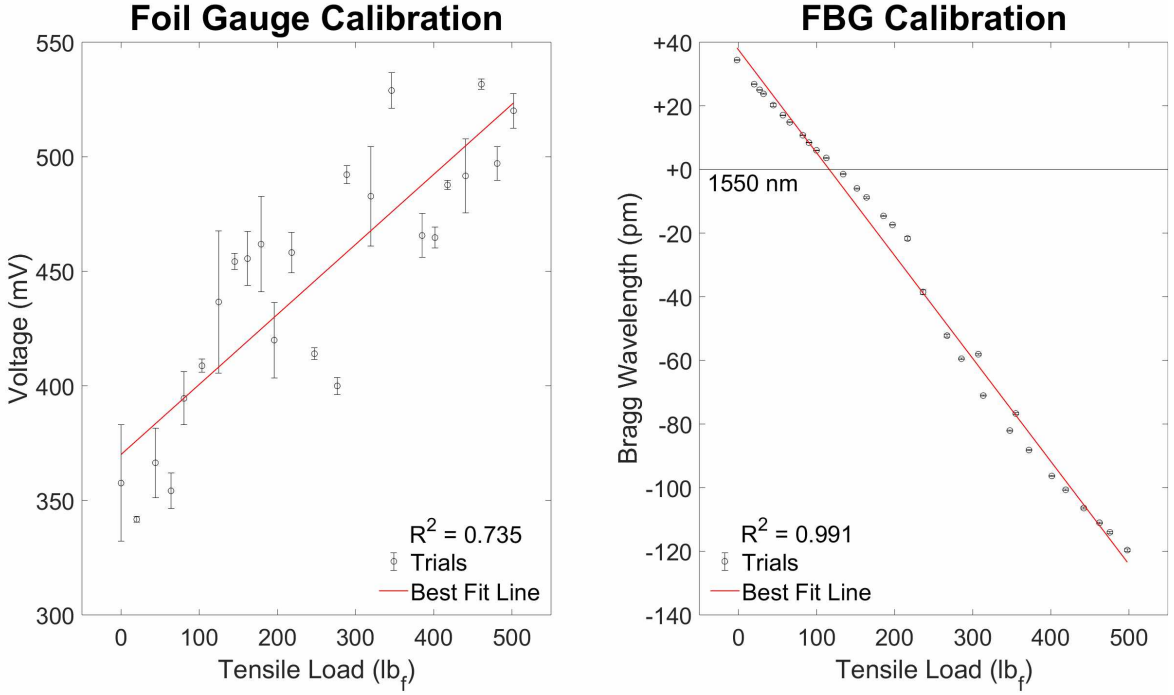


Figure 23: Resulting calibration best fit lines for the known linear response of both the foil gauge system and fiber Bragg grating system.

## 2.2.4 Signal Analysis

### 2.2.4.1 Despiking

As described in the introduction, the EMI emitted from the motor is visualized in a series of spikes. These spikes are picked up by the foil gauges and are present in the data. To characterize the signal from the foil gauges, it is necessary to detect and remove the signal spikes. To remove the spikes from, or despike, the foil gauge data, a moving median filter with a threshold is utilized [1, 14]. The filter, originally described by *Brock 1986*[1], first sorts through the data, obtaining the difference,  $D_i$ , of each data point,  $X_i$ , with a moving median filter output,  $Y_i$ . This median filter has a window size of  $2N + 1$ , where  $N$  is the filter order and  $i$  is the index. The differences are then binned, forming an empirical distribution. The spikes are detected as outliers in this distribution. The first zero count bin away from the middle of the differences' distribution becomes the threshold,  $DT$ . This may require increasing the bin count until a zero-count bin is found outside the main central section of the distribution. Care must be taken to remain below the sampling resolution to avoid

Table 6: Filter specifications. Bin count for the despiking filter for each foil gauge signal and window size for the Savitzky-Golay filter for each fiber Bragg grating signal.

Angular Velocity <i>RPM</i>	500	750	1000	1600	2000	2400
Despiking Bin Count	211	223	215	229	217	223
Savitzky-Golay Window Size	301	201	151	95	73	63

erroneous zero count bins. With the threshold set, the filter sorts through the data again, this time replacing the data point,  $X_i$ , with the moving median filter result,  $Y_i$ , whenever the absolute value of the difference,  $|D_i|$ , is greater than the threshold,  $DT$ . The logic of the algorithm is as follows:

$$X_i = Y_i \text{ if } |D_i| > DT \text{ else } X_i = X_i \text{ where } D_i = X_i - Y_i \quad (14)$$

For this experiment, a filter with the order of  $N = 3$  was used with the bin count for each foil gauge signal recorded in Table 6.

#### 2.2.4.2 Frequency Domain Filtering

To further filter the despiked foil gauge data, a Cauer bandpass filter was utilized. The filter passed  $\pm 5$  Hz on either side of the recorded revolutions per second of the motor, where the motor-flywheel combination vibrated with the largest amplitude due to an imbalance in the flywheel. This was only known and selected due to the information obtainable from the FBG data, otherwise such a seemingly arbitrary passed bandwidth would be moot.

#### 2.2.4.3 Time Series Filtering

Even though the FBG strain result is EMI free, the signal still has very low levels of noise. To filter this data, the Savitzky-Golay filter was utilized [12, 9]. This filter operates by convoluting a moving window of data points with an order specified polynomial:

$$Y_i = \frac{\sum_{j=-N}^N C_j X_{i+j}}{n} \quad (15)$$

Where  $Y_i$  is the filter output at index  $i$ ,  $X_{i+j}$  is the data point at the location  $i + j$ , and  $C_j$  is the polynomial coefficient determined by the specified filter order.  $n$  is the total elements in the window size  $2N + 1$ .

The main advantage of this filter is its retention of higher order statistical moments in the signal. The Savitzky-Golay filter preserve the second and higher order statistical moments, depending on the filter order chosen [9]. This preservation is important for correctly measuring the signal to noise ratio. For this experiment, the window sizes are tallied in Table 6 and a filter order of 4 was selected.

## 2.3 Results

The datasets are analyzed in 1 second windows. Due to this time window in an environmentally controlled laboratory, the temperature was verified to be constant and temperature change effects were ignored. The flywheel, although factory balanced, was slightly out of balance, resulting in it tilting about its rotating axis while the motor ran. This tilting induced a vibration in the loading data as the cylinder load cell began to act as a bending beam along the longitudinal axis. A perfectly balanced flywheel would result with a constant 28.5 lbf in the signal. However, as the motor spins, the sensors are subjected to compression and tension in a circular fashion. This creates a harmonic response about the static 28.5 lbf load of the flywheel/motor combination on the load cell and is visible in the Figure 24. The vibration matched perfectly to the motor RPM, which is confirmed with the maximum peak of the FBG signal in the frequency domain (Figure 25). Similarly, the filtered foil gauge frequency domain series shows a peak at the motor RPM (Figure 27) and a faint harmonic wave can be seen in the time series (Figure 26).

Keeping the vibration in mind, the foil gauge signal found in Figure 28 resembles the motor EMI more than it does the FBG signal. The foil gauge signal is riddled with spikes, where none exist for the FBG. Additionally, the spikes per second increases linearly with the motor speed (Figure 29 and Table 7), with a linear best fit line having a correlation coefficient of 0.938. This is consistent with the spikes originating from the motor EMI, as the increase in motor speed is proportional to the increasing number of pulsing square waves energizing the 28 poles (coils).

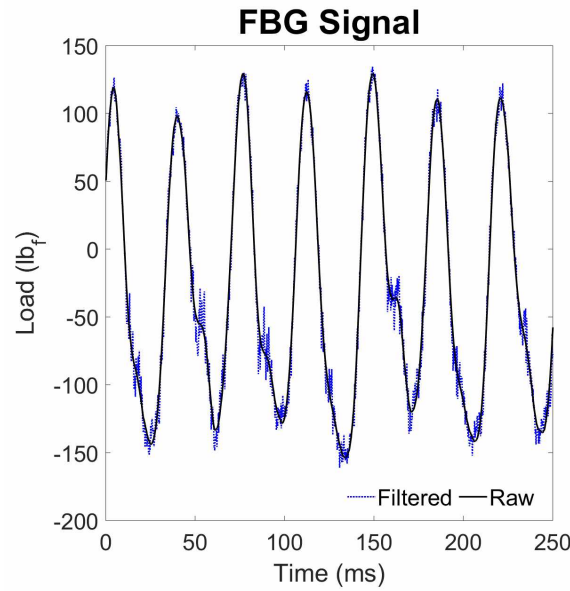


Figure 24: The fiber Bragg grating response with the motor operating at 1600 RPM, both raw and filtered. A 4<sup>th</sup> order Savitzky-Golay filter with a window size of 95 points was used to filter the signal.

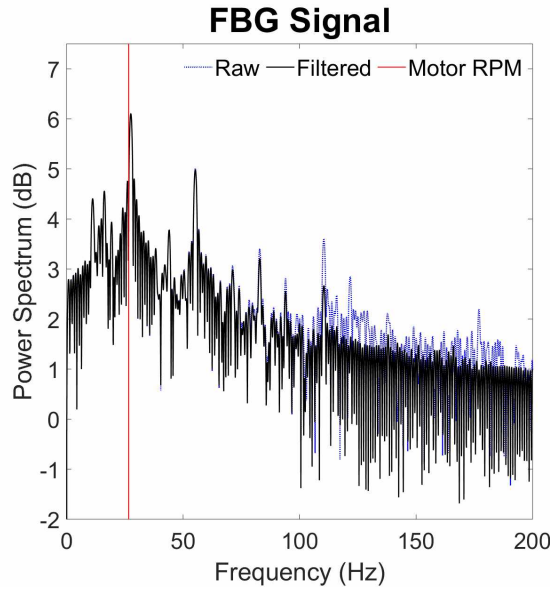


Figure 25: The frequency domain series of the fiber Bragg grating response found in Figure 24, both the raw and filtered data.

Table 7: Spikes per second at the corresponding motor RPM.

Angular Velocity <i>RPM</i>	500	750	1000	1600	2000	2400
Spikes per Second	87.1	166.8	203.1	238.2	311.8	329.0

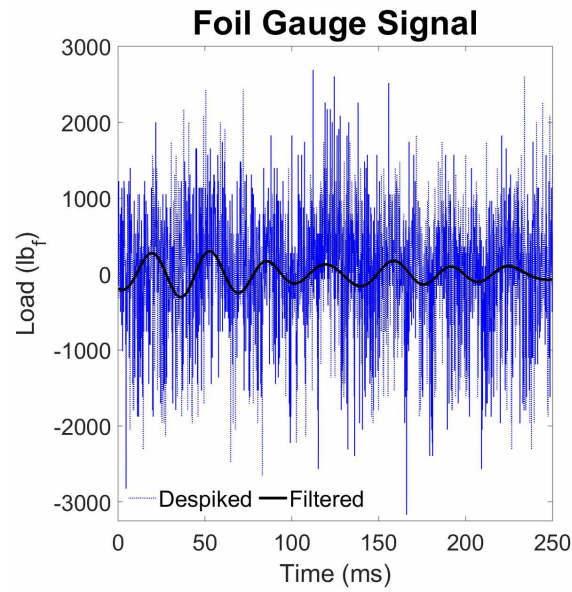


Figure 26: The foil gauge response with the motor operating at 1600 RPM, both despiked and filtered. A Cauer bandpass filter with a frequency window of 20 Hz around the motor RPM was used to filter the signal.

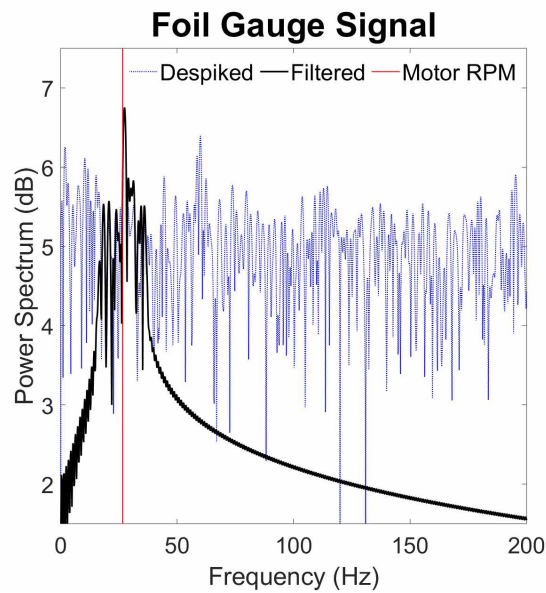


Figure 27: The frequency domain series of the foil gauge response found in Figure 26, both the despiked and filtered data, demonstrating the filter window.

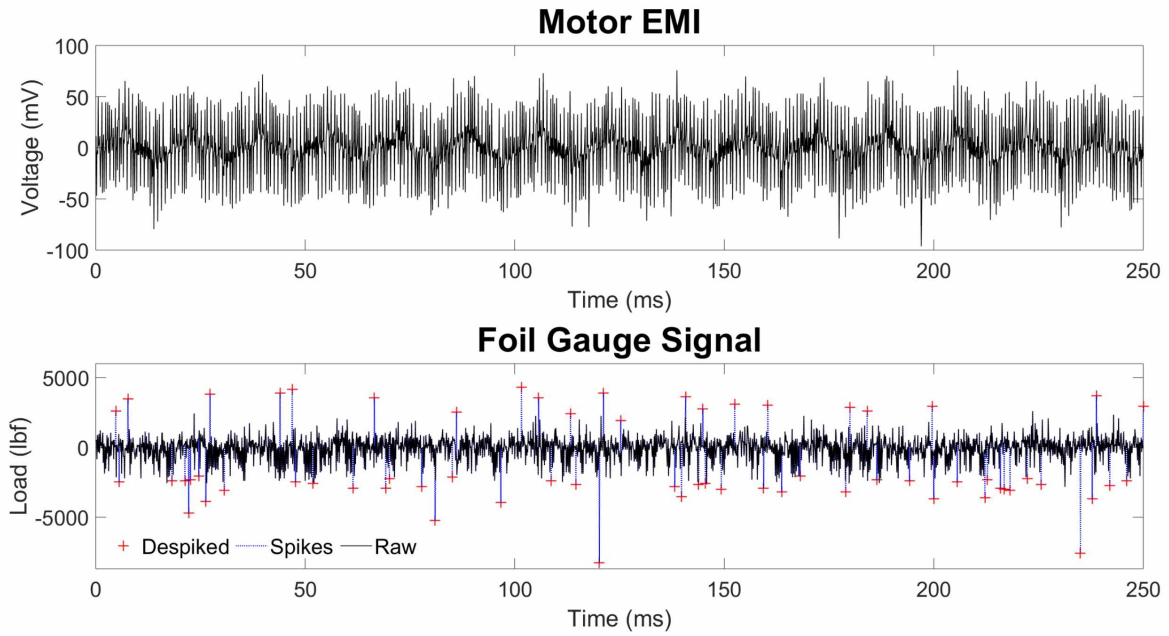


Figure 28: The motor EMI and foil gauge signal with the motor running at 1600 RPM. The raw and despiked signal are shown for the foil gauge with the removed spikes shown.

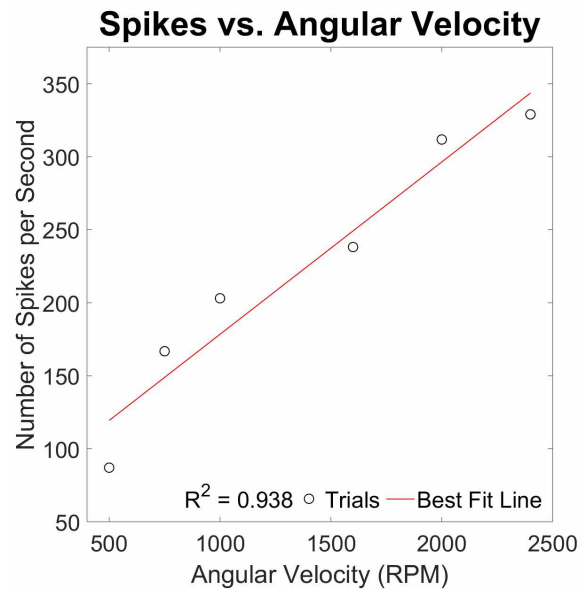


Figure 29: The spikes per second at different motor RPMs. There is a distinct linear increase of spikes with increasing motor angular velocity.

Table 8: Signal to noise ratio of all the datasets, foil gauge and fiber Bragg grating, at the corresponding motor RPM.

Angular Velocity <i>RPM</i>	500	750	1000	1600	2000	2400
Foil Gauge Signal Raw	0.0292	0.0282	0.0283	0.0292	0.0289	0.0279
Foil Gauge Signal Despiked	0.0443	0.0183	0.0100	0.0027	0.0113	0.0336
Foil Gauge Signal Filtered	0.0331	0.0087	0.0073	0.0035	0.0108	0.0038
Fiber Bragg Grating Signal Raw	25.7808	10.4722	2.0114	4.4868	4.3297	4.5082
Fiber Bragg Grating Signal Filtered	28.3387	10.6907	2.0929	4.5276	4.3413	4.5179

To determine the strength of the noise in each dataset, the signal to noise ratio (SNR) was calculated:

$$SNR = \frac{\mu}{\sigma} \quad (16)$$

With  $\mu$  and  $\sigma$  as the mean and standard deviation of the signals, respectively. The SNR for each signal set is presented in Table 8. The foil gauge signals have a SNR consistently below 0.05, with the smallest SNR at 0.0027, for the despiked data. Conversely, the FBG signals all have a SNR above 2, with the largest SNR at 28.34 for the filtered data.

## 2.4 Discussion

The foil gauge signal is affected by the EMI. Not only does the EMI appear as spikes in the signal but there is also pervasive, lower amplitude noise skewing the data. This can be seen in Figure 28 where even after the despiking process, the signal is very noisy and does not resemble the true mechanical signal seen in the FBG data. The foil gauge signal is degraded in the presence of the EMI emitted by the motor, which is conveyed by the low SNR values. To extract the low frequency mechanical signal from the dense noise, further filtering of the signal with a bandpass filter centered around the known frequency response, given by the FBG, is needed (shown in Figure 26 and 27). Without this frequency provided by the FBG, the mechanical signal would be indistinguishable from the noise in the foil gauge data, preventing any meaningful loading analysis from being performed. It should be noted that other modes of vibration are present in the FBG signal as well, which are lost in the foil gauge with the filtering. Again, what is easily perceptible by the high SNR FBG signal, is hidden in the foil gauge signal.

## 2.5 Conclusion

With the prevalence of electrical motors in the ground transportation industry, the drive to bring this method of propulsion to aerospace is increasing. However, to bring this technology to this field, safe stationary testing first needs to be performed to characterize it. The challenge that electric motors bring to this research is their emittance of electromagnetic interference, which affects sensing systems in ways that prior methods of propulsion did not.

To begin to quantify the effect of EMI on foil gauges, a load cell was developed implementing both the foil gauge technology and fiber Bragg grating technology. This provided the ability to separate the signal originating from the EMI and the signal originating from the mechanical loading. Here a brushless DC motor provided the EMI perturbation. Accordingly, a flywheel was utilized to provide the mechanical loading.

In the context of EMI emitted by electric motors, foil gauges require more effort in signal processing to discern relevant mechanical loading information. Such information may be impossible to extract if prior knowledge about the system isn't available. For example, in this testing, the vibration caused by the motor/flywheel wobbling isn't distinguishable from surrounding noise in both the time series and frequency domain representation of the data. The FBG on the other hand, returns the mechanical loading signal with a decent SNR.

The main downside to FBG strain sensing is cost of the system and sensors. At this time, a WDM FOSS with fiber Bragg grating sensors costs roughly 10 times as much as a comparably capable foil gauge setup. New developments in fiber optics may reduce this ratio.

For applications relatively free of EMI, or in applications where the EMI can be effectively mitigated, foil gauges operate well, as seen by the calibration tests performed here. However, from the perspective of the experimental results and discussion, the FBG interrogated by the WDM FOSS is the preferred method in comparison to foil gauges to sense a mechanical loading in the presence of EMI from an electrical motor. They are immune to EMI and featured a load sensitivity 4 times greater than the foil gauge with the load cell design presented.

## References

- [1] Brock, F. V., *Journal of Atmospheric and Oceanic Technology* **3**, 51 (1986).
- [2] Dally, J. W. and Riley, W. F., *Experimental Stress Analysis*, 3rd ed. (College House Enterprises, LLC, Knoxville, Tennessee, 1991).
- [3] Figliola, R. S. and Beasley, D. E., *Theory and Design for Mechanical Measurements*, 5th ed. (John Wiley & Sons, Inc., Hoboken, New Jersey, 2011).
- [4] Juvinall, R. C. and Marshek, K. M., *Fundamentals of Machine Component Design*, 5th ed. (John Wiley & Sons, Inc., Hoboken, New Jersey, 2012).
- [5] Kersey, A. D., Davis, M. A., Patrick, H. J., LeBlanc, M., Koo, K. P., Askins, C. G., Putnam, M. A., and Friebel, E. J., *Journal of Lightwave Technology* **15**, 1442 (1997).
- [6] Krohn, D., MacDougall, T., and Mendez, A., *Fiber Optic Sensors: Fundamentals and Applications*, 4th ed. (Society of Photo-Optical Instrumentation Engineers, Bellingham, Washington, 2014).
- [7] Lee, B., *Optical Fiber Technology* **9**, 57 (2003).
- [8] Ott, H. W., *Noise Reduction Techniques in Electronic Systems*, 2nd ed. (John Wiley & Sons, Inc., New York, 1988).
- [9] Press, W. H., Teukolsky, S. A., Vetterling, W. T., and Flannery, B. P., *Numerical Recipes: The Art of Scientific Computing*, 3rd ed. (Cambridge University Press, Cambridge, United Kingdom, 2007).
- [10] Rice, R. C., Jackson, J. L., Bakuckas, J., and Thompson, S., “Metallic materials properties development and standardization,” resreport (Federal Aviation Administration, U.S. Department of Transportation, 2003).
- [11] Samuel, A. and Lin, Y., in *51st AIAA/SAE/ASEE Joint Propulsion Conference* (Orlando, Florida, 2015).

- [12] Savitzky, A. and Golay, M. J. E., *Analytical Chemistry* **36**, 1627 (1964).
- [13] Solecki, R. and Conant, R. J., *Advanced Mechanics of Materials* (Oxford University Press, New York, New York, 2003).
- [14] Starkenburg, D., Metzger, S., Fochesatto, G. J., Alfieri, J. G., Gens, R., Prakash, A., and Cristobal, J., *Journal of Atmospheric and Oceanic Technology* **33**, 2001 (2016).
- [15] Timoshenko, S. P. and Goodier, J. N., *Theory of Elasticity* (McGraw-Hill, Inc., New York, 1970).



### 3 Concluding Statement

With the prevalence of electrical motors in the ground transportation industry, the drive to bring this method of propulsion to aerospace is increasing. To bring this technology to the aerospace field, safe stationary testing needs to be performed first to characterize it. The challenge that electric motors bring to this research is their emittance of electromagnetic interference, which affects susceptible sensing systems used for the sensing, navigation, and control of aerospace vehicles in ways that prior methods of propulsion did not.

Electromagnetic interference was described in general terms as well as in the terms of the brushless DC motor used in this research. A brief introduction to the different load cell types in industry was given. It was noted that foil gauge based load cells are the most common in aerospace, due to their ability to measure high frequency dynamic loads and lighter weight in comparison to the other types. The two strain sensors in question were described, highlighting the different phenomena utilized to observe strain. The primary difference of concern for this research is the foil gauges susceptibility to EMI and the immunity the fiber Bragg grating has. The appropriate accompanying systems necessary for the two sensors was also summarized, noting the advantage that fiber based sensing technology has in terms of distributive sensing.

Multiple iterations of design were needed to converge on an effective load cell concept for the test. This was finalized with the hollow cylinder design implementing both types of strain sensors that could accurately measure thrust with the presence of torque. The sensitivity of the design allowed for suitable determination of the dynamic mechanical loading. A description of the mathematical methods utilized for analysis was presented, highlighting the use of a modified median filter for despiking, the Savitzky-Golay filter for time series filtering, and an elliptic bandpass filter for frequency domain filtering.

In the context of EMI emitted by electric motors, foil gauges require much more signal processing to discern relevant mechanical loading information. Such information may be impossible to extract if prior knowledge about the system isn't available. For example, the vibration caused by the motor/flywheel wobbling isn't distinguishable from surrounding noise in both the time series and frequency domain representation of the data. The FBG on

the other hand, returns the mechanical loading signal with a decent SNR.

From the perspective of the this experiment's results and discussion, the FBG interrogated by the WDM FOSS is the preferred method to sense a mechanical loading in the presence of EMI from an electrical motor.

## 4 Appendix

### 4.1 MATLAB Code

#### 4.1.1 Load Cell Analytical Stress, Strain, and Resolution

```
clear all;

%Load Cell
E = 10.7e6; %Young's Modulus
nu = .33; %Poisson's Ratio
ri = 1; %Inner radius
ro = ri + .01; %Outer radius
A = pi()* (ro^2 - ri^2); %Cross sectional area of the load cell
J = pi() / 2 * (ro^4 - ri^4); %Polar moment of the load cell

%Forces and Stresses
P = 700; %lbf
T = 150; %lbf in

o = P/A; %axial normal stress
% tau = 150*ro/J; %axial shear stress
tau = 0;
oe = (o^2 + 3*tau^2)^.5; %von Mises stress
e = o/E;

%Wheatstone Bridge and foil gauges
GF = 2.105; %Gage factor
Vs = 10; %Bridge excitation voltage
Vo = Vs*GF/4*(1+nu)*e;
```

```
%FOSS
lambda = 1550;

%Resolution
reso = .001; %Oscilloscope resolution V
ereso = reso*4/(50*Vs*GF*(1+nu)); %Osc. strain res.
Po = ereso*E*A %Foil gauge sensitivity
uncPo = Po*.02 %Osc. uncertainty

resf = .001; %FOSS resolution nm
eresf = resf/(lambda*.78); %FOSS strain res.
Pf = eresf*E*A %FOSS sensitivity
uncPf = Pf*1 %FOSS uncertainty
```

#### 4.1.2 Load Cell Calibration Script

```
clear;
load('foil_cal.mat');
foil_l = 1;
foil_fit = fitlm(v,foil_l,'linear');
%linear fit with voltage as the independent variable as it will be later on

load('foss_cal.mat');
foss_l = 1;
foss_fit = fitlm(wv1550,foss_l,'linear');
%again linear fit with wavelength as the dependent variable

save('load_cell_function.mat','foil_fit','foss_fit');
```

#### 4.1.3 Fiber Bragg Grating Data Loader

```
clear;
```

```

load('load_cell_function.mat')
k = 1;

a = dir('*.*mat');
a = {a.name};

for i = 1:6

    load(a{i});
    foss{k}.test = str2double(a{i}(end-26:end-25));
    disp('-----');
    disp(foss{k}.test);

    foss{k}.load = feval(foss_fit,wvssload(1:end-1));
    foss{k}.rpm = str2double(a{i}(end-23:end-20));
    foss{k}.cps = foss{k}.rpm/60; %cycles per second
    foss{k}.rad = foss{k}.cps*2*pi; %angular frequency in radians

    win = round(5000/(2*foss{k}.cps));
    if mod(win,2) == 0
        win = win + 1;
    end

    filtered.load = sgolayfilt(foss{k}.load,4,win);
    filtered.window = win;
    foss{k}.filtered = filtered;

    clear wvssload;
    k = k + 1;
end

```

```
save('bf_foss.mat','foss');
```

#### 4.1.4 Foil Gauge Data Loader

```
clear;
```

```
k = 1;
```

```
a = dir('*.*mat');
```

```
a = {a.name};
```

```
for i = 3:8
```

```
load(a{i});
```

```
foil{k}.test = str2double(a{i}(end-26:end-25));
```

```
%loading the test number from test file name
```

```
disp('-----');
```

```
disp(foil{k}.test);
```

```
foil{k}.load = load_ss; %signal at steady state
```

```
foil{k}.rpm = str2double(a{i}(end-23:end-20));
```

```
%pulling test rpm from test file name
```

```
foil{k}.cps = foil{k}.rpm/60; %cycles per second
```

```
foil{k}.rad = foil{k}.cps*2*pi; %angular frequency in radians
```

```
foil{k}.gauge = 'foil';
```

```
clear load_ss;
```

```
k = k + 1;
```

```
end
```

```

for i = 1:6

    bin = [211,223,215,229,217,223]; %binning for despiking algorithm
    [data_out,spike_loc,spike_val] = brdespiking(foil{i}.load,3,bin(i));
    %despiking data

    despiked.load = data_out; %despiked data
    despiked.spike_loc = spike_loc; %spike locations
    despiked.spike_val = spike_val; %spike values
    despiked.bin = bin(i); %bin size used
    foil{i}.despiked = despiked;
    disp(length(spike_loc));

end

save('bf_foil.mat','foil');

```

#### 4.1.5 Motor Noise Data Loader

```

clear all;

k = 1;

a = dir('*.*mat');
a = {a.name};

for i = 1:6

    load(a{i});
    motor{k}.test = str2double(a{i}(end-13:end-12));
    %loading the test number from test file name
    disp('-----');
    disp(motor{k}.test);

```

```

u = [];

for j = 30:length(x) %joining 1 second measuring windows

    y = x{j};
    m = mean(y);
    y = y - m;
    u = [u,y];

end

motor{k}.noise = u; %loading motor noise
motor{k}.rpm = str2double(a{i}(end-10:end-7));
%loading the test rpm from test file nam
motor{k}.cps = motor{k}.rpm/60; %cycles per second
motor{k}.rad = motor{k}.cps*2*pi; %angular frequency in radians

clear wvssload;
k = k + 1;

end

save('motor.mat','motor');

```

#### 4.1.6 Signal to Noise Ratio Calculations

```

clear;

load('bf_foil.mat');
load('bf_foss.mat');

for i = 1:6

```

```

cps = foil{i}.cps;
foil_r = foil{i}.load(end-9999:end);
foil_dp = foil{i}.despiked.load(end-9999:end);
foil_f = bandpass(foil_dp,[cps-5 cps+5],1e4);
%bandpass filtering foil gauge data

snr_r(i) = abs(nanmean(foil_r)/nanstd(foil_r));
%SNR of raw foil gauge data
snr_dp(i) = abs(nanmean(foil_dp)/nanstd(foil_dp));
%SNR of despiked foil gauge data
snr_f(i) = abs(nanmean(foil_f)/nanstd(foil_f));
%SNR of filtered foil gauge data

foss_r = abs(foss{i}.load(end-4999:end));
foss_f = abs(foss{i}.filtered.load(end-4999:end));

snr_fr(i) = abs(nanmean(foss_r)/nanstd(foss_r));
%SNR of raw FBG data
snr_ff(i) = abs(nanmean(foss_f)/nanstd(foss_f));
%SNR of filtered FBG data

end

```

#### 4.1.7 Despiking Program

```

function [data_out,spike_loc,spike_val] = brdespiking(data_in,order,bin)
%despiking function Brock 1986 "A Nonlinear Filter to Remove Impulse Noise
%from Meteorological Data" JTECH

n = length(data_in);

```

```

j = -order:1:order;

y = nan(1,n);
dy = y;
data_out = data_in;
spike_val = y;
spike_loc = [];

mu = nanmean(data_in);
std = nanstd(data_in);
data = (data_in-mu)/std;

for i = (order+1):(n-order)
    y(i) = nanmedian(data(i+j));
    if i == order+1
        y(1:order) = y(i);
    elseif i == n-order
        y(n-order+1:n) = y(i);
    end
end

for i = 1:n
    dy(i) = data(i) - y(i);
end

[bin_count,bin_loc] = hist(dy,bin);
mid = (bin-1)/2+1;
k = NaN;
i = 1;

```

```

while isnan(k) && [(i+mid) <= length(bin_count) || (mid-i) >= 1]
    if bin_count(mid+i) == 0
        k = mid+i;
    elseif bin_count(mid-i) == 0
        k = mid-i;
    end
    i = i+1;
end

if isnan(k)
    return
else
    bin_width = bin_loc(2) - bin_loc(1);
    threshold = abs(bin_loc(k))-bin_width/2;

    for i = 1:n
        if abs(dy(i)) > threshold
            data_out(i) = y(i);
            spike_val(i) = data_in(i);
            spike_loc = [spike_loc,i];
        else
            data_out(i) = data(i);
        end
    end

    data_out = data_out*std+mu;
end
end

```